

Performance Study of a sMDT Prototype Chamber for the HL-LHC ATLAS Muon Detector Upgrade

K. Nelson,^{a,1} Y. Guo,^a D. Amidei,^a and E. Diehl^a

^a*Department of Physics, University of Michigan,
450 Church Street, Ann Arbor, MI 48109, USA*

E-mail: kevin.nelson@cern.ch

ABSTRACT: The High Luminosity Large Hadron Collider (HL-LHC) operations requires the experiments at the LHC to upgrade the detectors with new technologies to cope with much increased event rates. A new small-diameter Monitored Drift Tube (sMDT) chamber has been developed to upgrade the muon spectrometer of the ATLAS experiment. A prototype sMDT chamber has been constructed at the University of Michigan to demonstrate the required performance. Using cosmic ray muons the sMDT tracking resolution of $103.7 \pm 8.1 \mu\text{m}$ was measured, to be compared with a designed resolution of $106 \mu\text{m}$. The average tracking efficiency of $(98.5 \pm 0.2)\%$ was also measured. The methodology used to determine the detector tracking resolution and efficiency, which includes a reconstruction of sMDT data and a simulation of the test chamber with Geant4 is presented in detail. Further tracking resolution improvement has been evaluated when using the new high-gain readout electronics.

KEYWORDS: Muon spectrometers, Wire chambers, Detector modelling and simulations I

¹Corresponding author.

Contents

1	Introduction	2
2	Methodology	4
2.1	Test Stand	4
2.2	Data Acquisition	4
2.3	Data Analysis	4
2.4	Resolution	11
2.5	Efficiency	12
2.6	BIS Module 0 and ASD 2	13
3	Multiple Coulomb Scattering	13
3.1	Geant4 Simulation	13
3.2	Simulation of the Cosmic-Ray Spectrum	15
3.3	Deconvolution of Multiple Scattering Effects	16
4	Systematic Uncertainty Estimation	17
4.1	Auto-calibration and $r(t)$ parameterization	17
4.2	Track Fitting	17
4.3	Soft-Electron Component of Cosmic-Ray Spectrum	18
4.4	Time Slew Correction	20
4.5	Signal Propagation Time	21
4.6	Systematic uncertainties on efficiency measurement	24
5	Results	24
5.1	Single-Hit Resolution	24
5.2	Efficiency	26
6	Conclusions and Future Work	28
A	Matrix Inversion Chi Square Minimization	28
B	Likelihood Ratio Technique for Propagation of Errors	29
	Bibliography	30

1 Introduction

The planned HL-LHC upgrade will significantly increase the luminosity, and thus hit rate, for all particle detector systems on the experiments at the LHC, including the ATLAS [1] experiment’s muon spectrometer [2]. The current ATLAS muon spectrometer employs several detector technologies, including Resistive Plate Chambers (RPCs), Thin Gap Chambers (TGCs), Cathode Strip Chambers (CSCs), and Monitored Drift Tubes (MDTs). The ongoing Phase-I muon upgrade is to replace the Small-Wheels of the end-cap muon spectrometer with new Small-Wheels. Each new Small-Wheel consists of eight layers each of Micromegas and small-strip Thin Gap Chambers (sTGC), both providing trigger and tracking capabilities. The HL-LHC muon detector upgrade will replace the barrel inner MDT small sectors with the small-diameter monitored drift tube (sMDT) chambers and add a triple-layer thin-gap RPC in order to improve the muon trigger efficiency [3].

While upgrading the MDT chambers we must maintain spatial resolution. High spatial resolution in the ATLAS muon system is critical to measuring the momentum of muons produced in LHC collisions. Muons have a long enough lifetime to exit the ATLAS detector and will not deposit their energy fully in the calorimeter systems. High spatial resolution on the trajectory of muons allows for a momentum calculation by measuring the bending of the muon trajectory due to the ATLAS detector’s magnetic field. A new generation of the precision muon detector, sMDT chamber, has been developed at the Max Planck Institute (MPI) to upgrade the muon spectrometer [4].

The sMDT employs tubes with a 7.5 mm radius (compared to 15 mm for the original MDTs) to cope with higher hit rate and to make space for the new RPC layer. Compared to the ordinary MDTs the gas admixture is identical (93:7 % Ar:CO₂) and while the gas gain (2×10^4) is identical, the operating high voltage is 2730 V for sMDTs compared to 3080 V for MDTs.

We constructed a test chamber at the University of Michigan in summer 2018. This chamber is similar to the so-called BMG¹ chambers [5] which were installed in the ATLAS detector during 2017. After the prototype chamber was constructed, we performed intensive tests to evaluate the chamber performance. In winter 2021, a dry run for mass production of sMDT chambers was completed. The chamber produced, dubbed “module 0”, is shown in figure 1.

Our work has been to develop the methodology and code to analyze raw data collected with cosmic-ray runs and to simulate the sMDT chambers with Geant4. In this document we will outline the results and describe the methodology used to reconstruct and simulate cosmic-ray muon events using both the BMG prototype chamber and the BIS-type module 0 chamber. The BMG chamber is an early prototype and the BIS module 0 chamber is a dry run for the chamber construction process at the University of Michigan. Over the next three years 48 sMDT chambers will be produced at the University of Michigan and shipped to CERN to be installed in the ATLAS detector. In parallel, our collaborators at MPI will construct 48 sMDT chambers and have already supplied 14 sMDT chambers to ATLAS (2 BME, 12 BMT). The prototype and module 0 chambers use the same principle but have different geometries (differing drift tube length, number of tubes and spacing between the multilayers). Sections 2, 3 and 4 describe the procedure as carried out on the BMG

¹Chambers in the ATLAS muon spectrometer are named (in part) by location and size. BMG stands for Barrel (the region $|\eta| < 1.05$), Middle (of the three layers), Gap (filling a previously existing gap between chambers in the spectrometer). BIS stands for Barrel Inner Small.



Figure 1: The module 0 chamber produced at the University of Michigan. The readout electronics are shown mounted on one end of the drift tubes. The other end of the tubes are fitted with high-voltage distribution boards. The chamber is approximately 0.2x1.1x1.5 meters in size.

prototype. The procedure was also applied in an identical manner to the module 0 chamber. Results for both chambers are reported in section 5.

2 Methodology

2.1 Test Stand

The cosmic-ray test stand contains a prototype of a sMDT BMG chamber for the muon spectrometer on the ATLAS experiment. The chamber consists of two sets (multilayers) of 4 layers of 54 tubes each, with a spacing of roughly 18 cm between the two multilayers. The tubes are made of aluminum and have a wall thickness of 0.4 mm. A more complete summary of the sMDT geometry and a comparison to the MDT design can be found at [4].

For the prototype chamber only a portion of the test stand was instrumented due to limited availability of readout electronics. Therefore, only 24 of the 54 total tubes in each layer are read out using the data acquisition system. The reduced fiducial volume naturally constrains tracks to be within an angle of 45 degrees with respect to the vertical, because a track is required to have hits in each multilayer. The results for module 0 use a fully instrumented chamber.

2.2 Data Acquisition

The data acquisition (DAQ) system uses a high performance time to digital converter (HPTDC) [6] to digitize drift time information. The DAQ is triggered by a large ($\approx 1.5 \text{ m}^2$) scintillator mounted above the test chamber with photo-multiplier tubes (PMTs) mounted on each end. To trigger readout of the HPTDC chips, coincidence of the two PMTs is required. Triggering on cosmic-rays via scintillator PMTs has a significant trigger time smearing due to the large size of the scintillator, as will be addressed in section 2.3. Cosmic-ray muon signals are collected by the front-end electronics mezzanine cards containing the ASD[7] and HPTDC chips. The ASD has a threshold of ≈ 24 primary ionization electrons corresponding to an electronics signal threshold of 39 mV. The HPTDC digitizes the ionization electron drift time.

2.3 Data Analysis

The data analysis methodology developed in this work encompasses reconstructing raw data and simulating the multiple scattering of cosmic-rays. The analysis strategy is as follows. First, we decode raw binary data-words output by the DAQ system. We then perform a calibration of the $r(t)$ function, which is parameterized as a 10-degree Chebyshev polynomial. We then fit straight, 2-D tracks in the plane perpendicular to the wires and create distributions of biased and unbiased residuals. To account for multiple coulomb scattering, which is much more significant for cosmic-rays than muons in the ATLAS cavern with $\geq 20 \text{ GeV}$ of p_T , residual distributions are deconvoluted with a Monte Carlo (MC) truth multiple scattering residual distribution.² Finally, the spatial resolution is calculated.

We now describe the procedure in greater detail. The DAQ system runs in the triggered mode. Upon receiving a trigger from the scintillator, all matched hits are packaged as an event and written out by the DAQ. To filter out unexpected hits that are not related to a muon track, hits from adjacent tubes are merged into clusters and precisely one cluster is required in each multilayer. One cluster of precisely four hits is required in each multilayer, unless otherwise specified.

² $p_T \geq 20 \text{ GeV}$ is the cut used in the ATLAS MDT Run 2 resolution measurement [8].

A time slew correction is also applied to compensate for the timing variation caused by the signal amplitude. The time slew is a function of the response of the particular Amplifier/Shaper/Discriminator (ASD) chip used in the front-end electronics, as described in the corresponding manual (see figures 34 and 35 in [7]). After accounting for time slew, the corrected time has the form:

$$t_{\text{corrected}} = t - t_0 - 35.59\text{ns} e^{-ADC/61.33\text{ns}} \quad (2.1)$$

Where t is the time of the pulse, t_0 is the leading edge time from the fit to the drift time spectrum for a particular tube (defined in equation 2.2; for example see figure 2a), and ADC is the output pulse width of the ASD chip. Typical values for ADC are on the order of 100 nanoseconds, and typical values for the time correction are $\approx 6 \pm 2.5$ ns. The nonzero mean slew correction is irrelevant and will simply shift the fitted t_0 and t_{max} for each tube. t_{max} is the falling edge fit, defined in equation 2.3. After the event selection, t_0 and t_{max} values are fit from the drift time spectra for each tube. An example drift time spectrum is shown in figure 2a. The rising edge on the drift time spectrum is fit using a Fermi-Dirac step function:

$$b + \frac{A}{1 + e^{-(t-t_0)/T}} \quad (2.2)$$

where b is the background noise floor, A is the amplitude, T is the t_0 slope (rise time), and t_0 is the leading edge time that appears in equation (2.1). The falling edge t_{max} is fit using the function

$$b + \frac{e^{a+c(t-t_0)}}{1 + e^{(t-t_{\text{max}})/T}} \quad (2.3)$$

where b and t_0 are fixed to the values returned by the rising edge fit, T is the t_{max} slope (fall time) and t_{max} is the best fit maximum drift time. The total drift time is defined to be $t_{\text{max}} - t_0$, and these fits are performed for each drift tube. An example ADC spectrum is shown in figure 2b. The ADC distribution is fit using a skew normal distribution. Note that in order to cut noise, a threshold cut of 40 ns was imposed on ADC values.

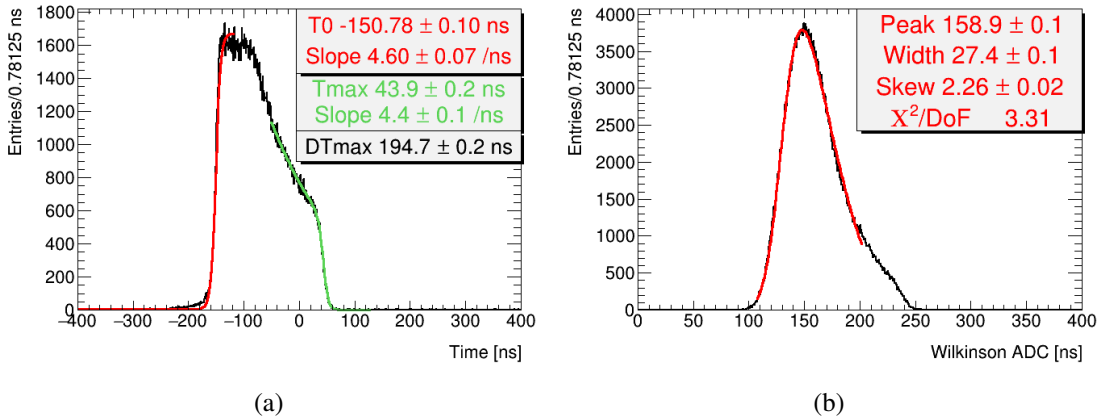


Figure 2: (a) Example drift time spectrum for one channel from a cosmic-ray data run collected on July 10, 2020. (b) Example ADC spectrum for the same channel.

Auto-calibration and track fitting are both performed using the matrix inversion chi-square minimization method (see [9] and appendix A). Auto-calibration is the process by which the parameterization describing the $r(t)$ function is updated iteratively. The auto-calibration algorithm iterates over two steps: (i) fitting tracks for set of events using a fixed $r(t)$ function and (ii) updating the $r(t)$ function using the matrix inversion method. The process continues until the parameterization of the $r(t)$ function converges. Auto-calibration requires knowledge of the resolution as a function of drift radius, which is precisely the quantity we wish to measure. We initialize the resolution as a function of drift radius to the value observed using legacy MDTs [8].

The $r(t)$ function is parameterized as a Chebyshev polynomial with 10 terms. Via the matrix inversion method we calculate the change to apply to each Chebyshev coefficient on each iteration of auto-calibration. Chebyshev functions are defined on the domain $[-1,1]$, so we linearly scale the domain of the Chebyshev functions to $[t_0, t_{\max}]$ for the individual t_0, t_{\max} for each tube. A robust means of validating this procedure is to compare the chi-square distribution obtained to the expected one with the same number of degrees of freedom. In this analysis, events with eight hits are used and a track is parameterized with three degrees of freedom (as will be discussed in more detail), leaving five remaining. The chi-square distribution obtained from the track fits using the auto-calibrated $r(t)$ function is shown in figure 3, compared to a chi-square distribution with five degrees of freedom. The non-closure in the tail is likely the result of multiple coulomb scattering, which is not accounted for at this stage in the analysis, but will be addressed in section 3.3. The angular distribution for all fitted tracks is shown in figure 4. The wide angular distribution, in conjunction with the agreement between expectation and observation in the chi-square distribution, demonstrates the efficacy of the tracking algorithm. An angular distribution that is too narrow, for example only selecting near-vertical tracks, is a possible indication of a false minimum in the $r(t)$ function autocalibration. Such a case is not observed.

The $r(t)$ function for a data run from July 10, 2020 is shown in figure 5. The error band is the resolution as a function of radius, shown in figure 25. Figure 6 shows actual and percent difference between the $r(t)$ function shown in figure 5 to an MDT $r(t)$ function from the gas monitor chamber at CERN [10]. The $r(t)$ functions are not expected to agree exactly due to slightly different operating conditions (temperature, pressure). The $r(t)$ can be calibrated from a reference and knowledge of the differences in these conditions, as is done with the gas monitor[10] and chambers in the ATLAS cavern. The comparison to an existing $r(t)$ simply aims to show the general level of agreement, both validating our in-situ observation of the $r(t)$ function and demonstrating the order of magnitude of the environmental factors on the $r(t)$ function. The percent difference is higher than 5% for the 1 millimeter closest to the wire, where our $r(t)$ function is not constrained to go to zero for hits with zero drift time. This causes the percent difference to blow up, while the absolute difference remains below 150 microns, within the resolution in this regime. Over the entire domain the $r(t)$ functions differ on the order of 100 microns, which is on the order of the resolution of the chamber. The Michigan test chamber setup does not record real-time temperature, humidity, or pressure data. These three factors will all influence the $r(t)$ function, meaning without this information we must use auto-calibration to derive an $r(t)$ function for each data run while remaining agnostic to the precise data taking conditions.

We will now describe the track fitting procedure in more detail. The first step is to find an initial guess via some pattern recognition algorithm. If the chi-square minimization algorithm is

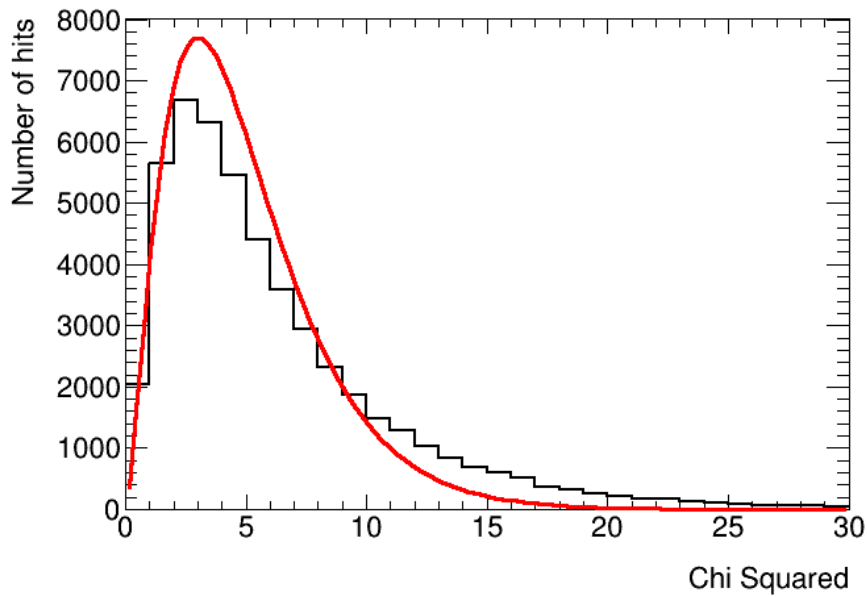


Figure 3: Chi-square distribution for fitted straight line tracks. The tracks are fit in a 2-D plane perpendicular to the wires, as shown in figure 8. The red curve shows the expected chi-square distribution, given the number of degrees of freedom, normalized to the same area as the histogram.

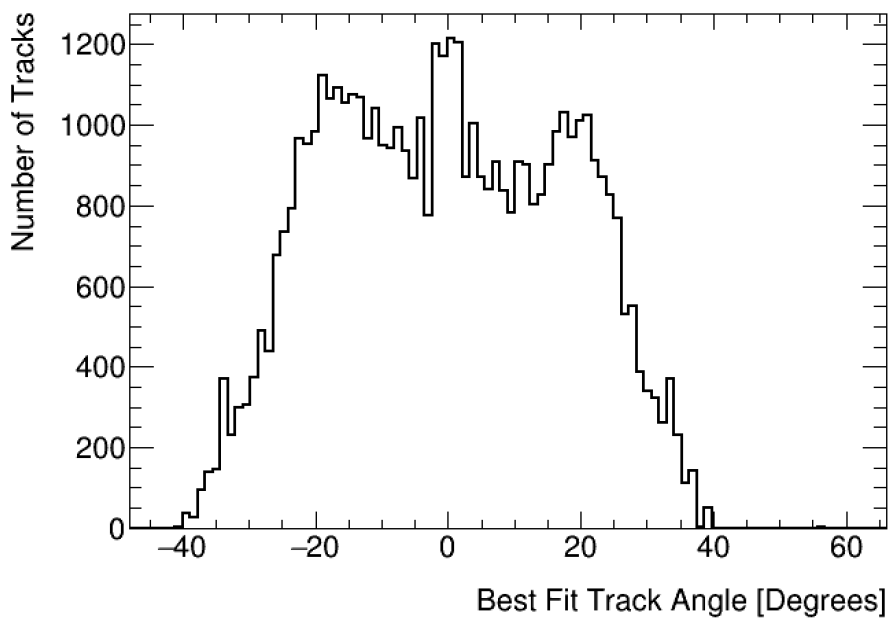


Figure 4: The angular distribution for all fitted tracks.

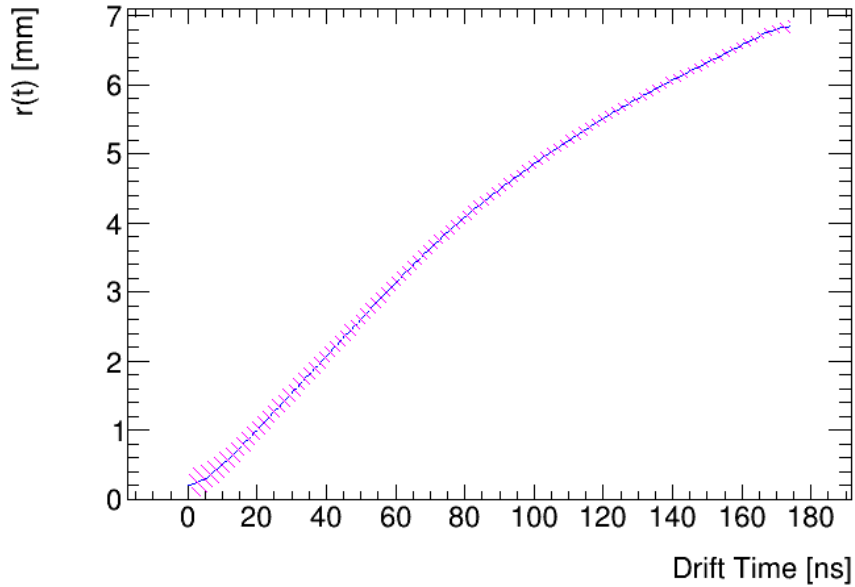


Figure 5: The auto-calibrated $r(t)$ function. Note that the Chebyshev polynomials are defined on the range $[-1,1]$ so we linearly scale this $r(t)$ function to $[t_0, t_{\max}]$ for each tube. Therefore, different tubes may have slightly different $r(t)$ functions if they have a differing maximum drift time $t_{\max} - t_0$. The hatched region represents the resolution as a function of radius presented in figure 25.

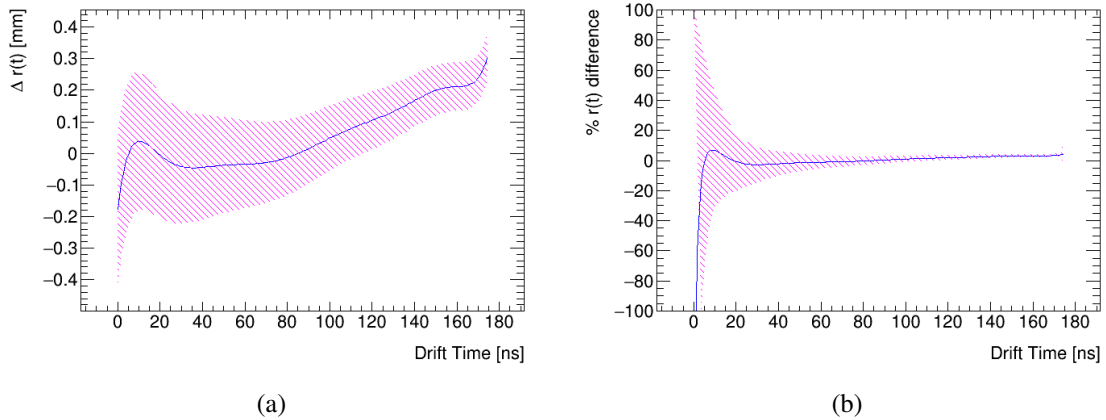


Figure 6: (a) Absolute and (b) percent difference in $r(t)$ functions between a truncated MDT $r(t)$ from the gas monitor chamber at CERN and the auto-calibrated $r(t)$ function derived in this work. The hatched region is the size of the final resolution as a function of radius presented in figure 25.

not initialized to a point close enough to the global minimum we risk getting caught in a local, but not global, chi-square minimum. The pattern recognition algorithm used in this work is a brute force method to decide if the track passes to the right or left of the wire. We try $2^{(n \text{ hits})}$ different combinations of hit location, displaced either to the right or left of the wire by the radial distance. The combination of right/left decisions that has the best chi-square is used to seed the slope and intercept of the track. For the first pass, the error used is the expected MDT resolution function [8]. After the radial resolution function is measured, we iterate the entire resolution procedure until the coefficients in table 4 converge.

Track fitting again uses the matrix inversion technique. Tracks are modeled in a 2-dimensional plane and can be parameterized as a straight line with an angle with respect to the vertical and x-intercept (see figure 8 for a definition of the x axis) as there is negligible magnetic field present. The choice of angle with respect to the vertical and x-intercept to describe a straight line avoids possible singularities in slope and y intercept for a purely vertical track. Additionally, tracks have a third parameter: a global time shift Δt_0 . The Δt_0 distribution shown in figure 7 is appreciably wider than the distribution observed in the Run 2 MDT resolution paper, which recorded an RMS width of 0.7 nanoseconds (see figure 9 in [8]). Unlike tracks in the cavern, which have the LHC clock to reference a collision time, we must reconstruct the trigger time. The large scintillator area (approximately 1.5 m^2) smears the timing information, as the incident cosmic-ray may be closer to one end of the scintillator, and thus closer to one PMT, to the other. As discussed in section 2.2, the coincidence of both PMTs is the trigger signal. So there may be some delay on the order of nanoseconds associated with the DAQ system, requiring an additional degree of freedom in the tracking.

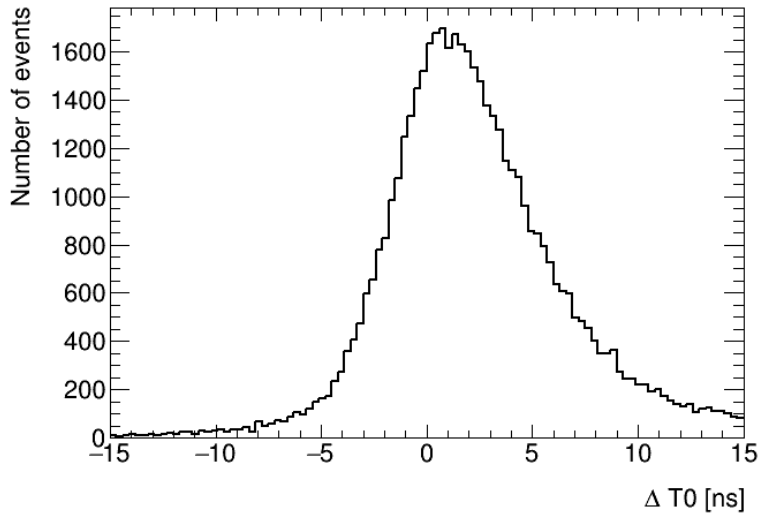


Figure 7: Δt_0 distribution from fit residual calculation for cosmic-ray data collected on July 10, 2020.

Tracks are fit using the current $r(t)$ function, and residuals from the best fit track inform the auto-calibration routine how to update the Chebyshev coefficients. An example event display with a fitted two-dimensional track is shown in Figures 8 and 9. An example biased (unbiased) residual

distribution is shown in figure 10 (11). The chi-square distribution for fitted tracks is shown in figure 3. The agreement is not perfect, with a slightly long tail that is perhaps the result of the multiple scattering, as will be discussed in section 3.

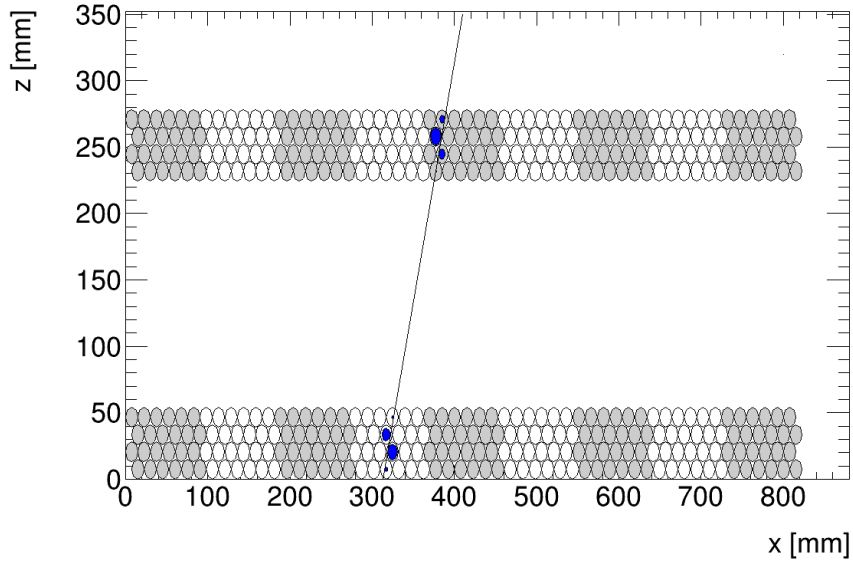


Figure 8: A single event with a straight line track fitted. The blue circles show the radius of each hit, which is determined using the auto-calibrated $r(t)$ function. The grey and white regions show the demarcations between different readout electronics cards.

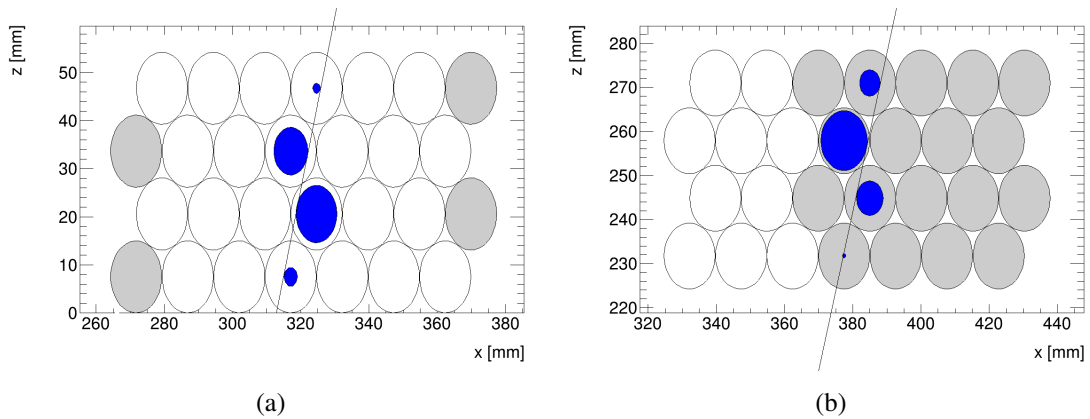


Figure 9: Close up of the (a) bottom and (b) top multilayers for the event shown in figure 8. The blue circles show the radius of each hit, which is determined using the auto-calibrated $r(t)$ function. The grey and white regions show the demarcations between different readout electronics cards. The black line is the track fit.

2.4 Resolution

After we created a calibrated $r(t)$ function we performed a resolution measurement. Using the calibrated $r(t)$ we fit a straight line track in the two dimensional plane perpendicular to the wires, with the additional event-by-event Δt_0 timing shift. Each hit has some residual, the difference between the hit radius and the radius predicted by the straight line fit. We created two different residual distributions, the biased and unbiased residuals. The unbiased residual is the residual for a given hit when it is excluded from the straight line track fitting procedure. The biased residual is the residual when a given hit is included in the chi-square minimization of the straight line track, which biases the fit to be closer to this given hit.

The quantities σ_b (biased width) and σ_u (unbiased width) are defined as the average width of a double gaussian fit to the corresponding residual distribution, weighted by the amplitude of each gaussian [8]:

$$\sigma_{[b,u]} = \frac{A_w \times \sigma_w + A_n \times \sigma_n}{A_w + A_n} \quad (2.4)$$

Where A is the amplitude of the gaussian, σ is its standard deviation, and the subscripts n and w are the narrow and wide gaussians of the double gaussian distribution. The double gaussian fit was constrained to have a common mean for the two gaussians. Example biased and unbiased residual distributions with double gaussian fits are shown in figure 10 and figure 11, respectively. The resolution σ is defined to be the geometric mean of the two residual distributions [8].

$$\sigma = \sqrt{\sigma_b \times \sigma_u} \quad (2.5)$$

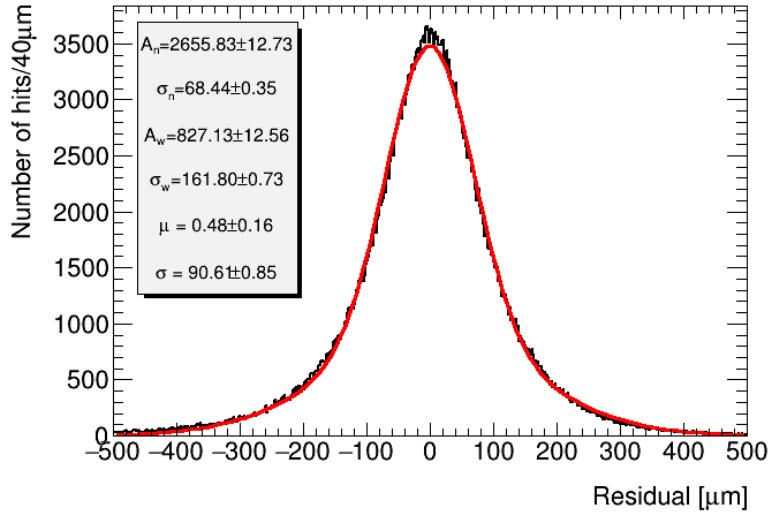


Figure 10: Biased residuals on cosmic-ray data taken July 10, 2020. The red curve shows the double gaussian fit. The fit parameters shown in the box are: A_n , σ_n = Amplitude and width of the narrow gaussian fit, respectively; A_w , σ_w = Amplitude and width of the wide gaussian fit, respectively; μ = common mean of wide and narrow fits; σ = the biased residual distribution width from eq. 2.4

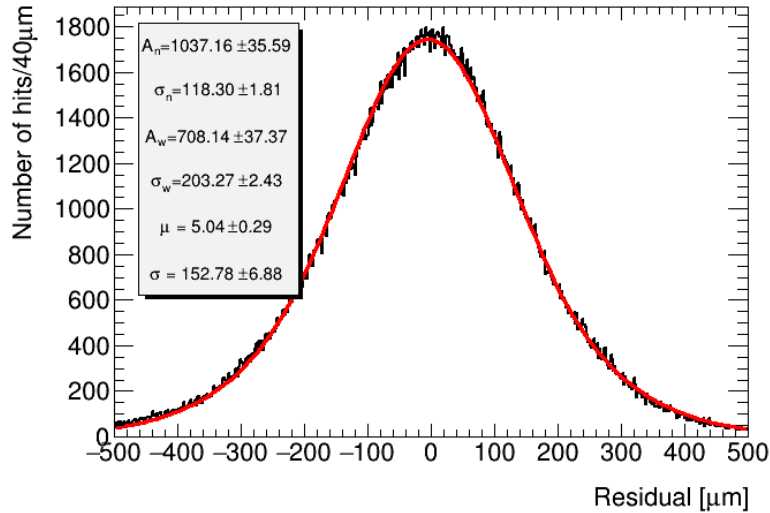


Figure 11: Unbiased residuals from cosmic-ray data taken July 10, 2020. The red curve shows the double gaussian fit. The fit parameters are the same as shown in figure 10 except σ = the unbiased residual distribution width using eq. 2.4

Applying equation (2.5) to the biased and unbiased residuals from the cosmic-ray data obtained on July 10, 2020 (see figures 10, 11), we found a single-hit resolution of $117.7 \pm 2.1 \mu\text{m}$. The quoted error is the statistical error from the fit parameters, propagated through equation (2.5). The primary reason for the tension with the expected resolution of $106 \mu\text{m}$ is multiple scattering of low energy cosmic-rays, as will be discussed in section 3.

2.5 Efficiency

The layer efficiency of the drift tubes is defined as the number of times a track passed through a layer and a hit was recorded divided by the number of times a track passed through a layer, regardless of whether a hit was recorded. The layer efficiency accounts for both the efficiency of the tubes in reconstructing hits and the dead regions due to tube walls and the gaps between tubes. We similarly define the tube efficiency, the number of times that a tube sees a hit divided by the number of times that a track passes through the gas volume of a tube. In order to calculate the layer and tube efficiencies, we relax the tight reconstruction cuts described in section 2.3, which were used for measuring the resolution (8 hits, 4 in each multilayer, were required. This would bias the efficiency measurement against clusters with a “hole” in them, which are of interest in the efficiency study.) To measure the efficiency, clusters of 1 to 6 hits in size are permitted, and events may have between 6 and 12 hits and up to 3 clusters per multilayer. These cuts accommodate events where tubes did not fire despite a track passing through the gas volume, while still maintaining enough hits to reconstruct a track.

We perform the entire reconstruction methodology on this new sample: decoding raw data, fitting the t_0 and t_{max} of drift time distributions, auto-calibration, and track fitting. We then calculate the number of times the best fit track went through the layer (or tube) and did or did not register a hit. When evaluating whether a track passes through a tube volume we leave that tube out of the

track fitting to not bias the fit to be closer to that tube, as is done to calculate the unbiased residual distribution. Hits greater than 5σ away from a track are not counted towards the efficiency.

2.6 BIS Module 0 and ASD 2

The entire procedure is repeated for the module 0 BIS chamber, which was produced at the University of Michigan in February 2021. We also used two different sets of readout electronics with module 0 to compare their performance. The first data taken with module 0 uses the legacy Amplifier/Shaper/Discriminator (ASD) 1 chip, the same electronics as used to test the BMG prototype. We then use the new ASD 2 chip [11] on module 0, which will be used for the detector readout electronics upgrade. The ASD 2 chip has approximately 50% higher gain than ASD 1, which increases the precision on the timing measurement and reduces the size of the slew effect. The results shown in section 5 shows the performance of module 0 with both the legacy and the new readout electronics.

3 Multiple Coulomb Scattering

3.1 Geant4 Simulation

In order to estimate the impact of multiple scattering, we created a Geant4 [12] simulation of the BMG-like chamber. The simulated geometry includes the tubes (walls, gas, and wires) and the spacer frame, which sits between the multilayers. The spacer frame represents a significant amount of material, and has a complex geometry. The 3D geometry of the spacer frame is described by the CAD software in a .stl file format and imported into Geant4 using the Geant Detector XML (GDML) markup language. Figures 12 and 13 show a simulated 1 GeV muon passing through the chamber using our Geant4 simulation.

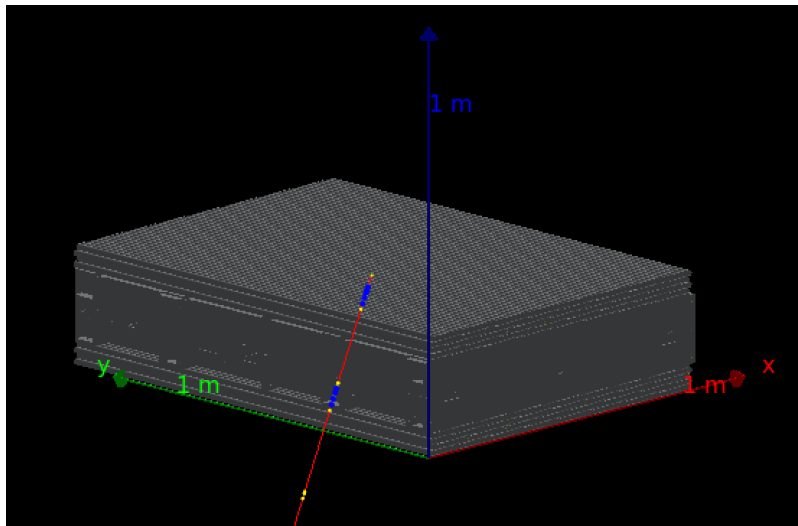


Figure 12: A 1 GeV muon passes through the simulated test chamber.

Using MC truth information for charged particles passing through the simulated gas volume, we reconstruct events, similarly to what is done from raw data. Thus, we can create a dataset with

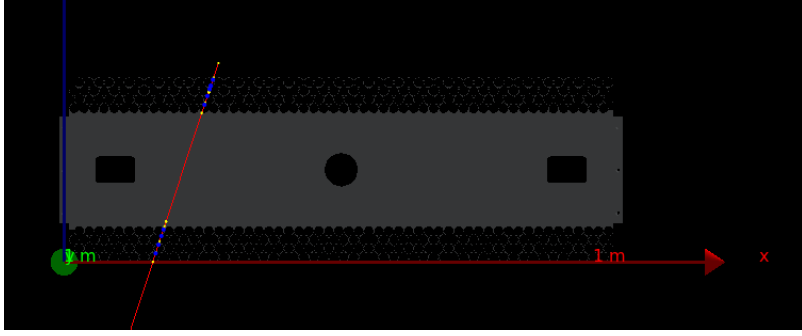


Figure 13: A 1 GeV muon passes through the simulated test chamber, this time shown from the angle along the direction of the wires.

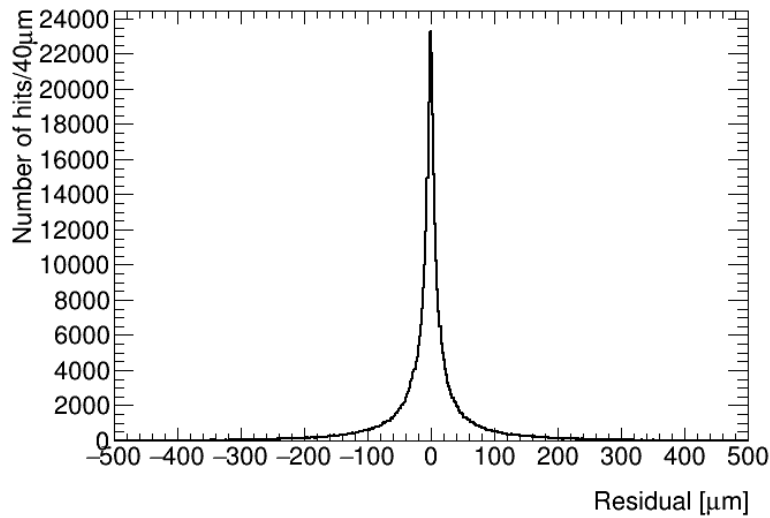


Figure 14: Residual distribution obtained from simulating multiple scattering of cosmic-rays passing through the test chamber. There is a sharp central peak and non-gaussian tails.

perfectly reconstructed hit radii. In practice the hit radii are reconstructed as the closest approach of any charged particle within the gas volume, so the effects of delta rays or any other energetic secondaries are included. This data is fed through exactly the same data analysis steps discussed in section 2.3 and section 2.4. The width of the residual distributions are solely the result of multiple scattering, since tube resolution has not been added to the monte carlo. For an example residual distribution see figure 14. Unlike the residual distribution observed in data, it is not well described by a double gaussian fit, but has a sharp central peak and non-gaussian tails.

As validation of the $r(t)$ calibration procedure, we have run on an MC truth dataset with 20 GeV muons which have very little multiple scattering, with hit radii reconstructed as described. Hit times are then created with the inverse $r(t)$ function of the gas monitor chamber, which is linearly interpolated in 1.9 ns bins. In such a test over 90% of the fit residuals are less than 10 microns, validating the ability of the autocalibration to capture a realistic $r(t)$ function.

Parameter	Value
A_1	0.3924
λ_1	5.5264
λ_2	1.4180

Table 1: Fitted parameters to equation (3.1) to describe the muon component of the cosmic-ray spectrum

3.2 Simulation of the Cosmic-Ray Spectrum

The effect of the multiple scattering is dependent on the assumptions on the particle and energy content of the cosmic-ray spectrum. Many particle species are present in cosmic-rays due to energetic electromagnetic and hadronic showers in the upper atmosphere. In this work we will simulate only the muon and soft-electron components of the cosmic-ray spectrum, which are the most significant components at sea level.

The Particle Data Group (PDG) article on cosmic-rays [13] provides data describing muon flux as a function of momentum at sea level. We found this data was well fit as the sum of two exponentials as seen in figure 15. The functional form of the probability distribution is described in equation (3.1), and the coefficients are listed in table 1. The PDG article also notes that the muon energy spectrum is roughly flat below 1 GeV, so the fit terminates at 0.6 GeV, where the data runs out, and we simulate the energy spectrum as flat below this cutoff.

$$\frac{A_1}{\lambda_1} e^{p/\lambda_1} + \frac{(1 - A_1)}{\lambda_2} e^{p/\lambda_2} \quad (3.1)$$

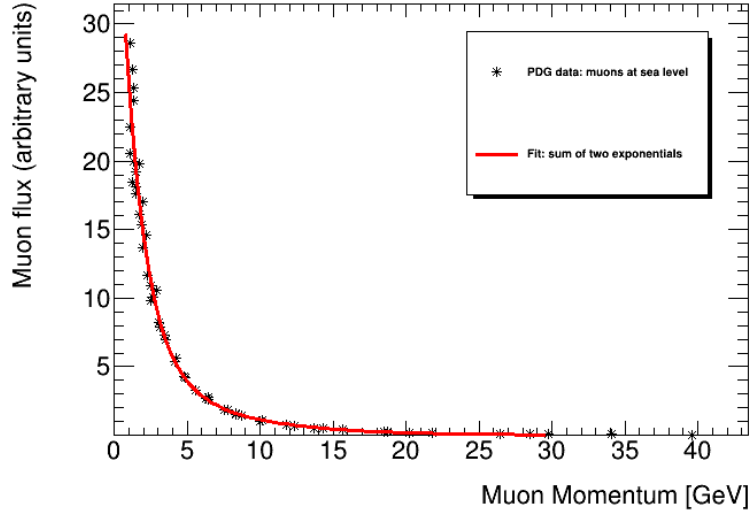


Figure 15: Probability distribution for muon flux at sea level. The sum of two exponential curves are fit to cosmic-ray data. For functional form, see equation (3.1). For fit parameters, see table 1.

The muon component described thus far is estimated to be 70% of the particle content. The remaining 30% of cosmic-rays are simulated as soft-electrons. This ratio is again informed by the

PDG article on cosmic-rays[13], which lists the intensity of cosmic-ray muons at sea level to be $\approx 1\text{cm}^{-2}\text{min}^{-1}$ and the intensity of electrons above 10 MeV to be $\approx 30\text{m}^{-2}\text{s}^{-1}\text{sr}^{-1}$. As discussed in section 2.1, cosmic-rays are naturally limited to an angle less than 45 degrees with respect to the vertical, which can be used to calculate 1.84 steradians as the angular coverage (assuming 2π phi coverage). Converting to a common unit, we find $\approx 166\text{m}^{-2}\text{s}^{-1}$ for cosmic-ray muons and $\approx 55\text{m}^{-2}\text{s}^{-1}$ for cosmic-ray electrons above 10 MeV, for a $\approx 25\%$ electron component. Therefore 30% is a conservative estimate of the electron component of the cosmic-ray spectrum, providing some room for error in our simple calculation. Ultimately, we will show in section 4.3 that the resolution is rather insensitive to the soft-electron fraction. The electron component is modeled as having a minimum energy of 10 MeV and as an exponential with a length scale of 50 MeV.

3.3 Deconvolution of Multiple Scattering Effects

The observed residuals presented in section 2.4 are a convolution of the true detector resolution and the multiple scattering residual distribution. With a MC truth multiple scattering residual distribution in hand, we can remove the effect of multiple scattering via deconvolution and estimate the resolution of this detector on high p_T muons in the ATLAS cavern.

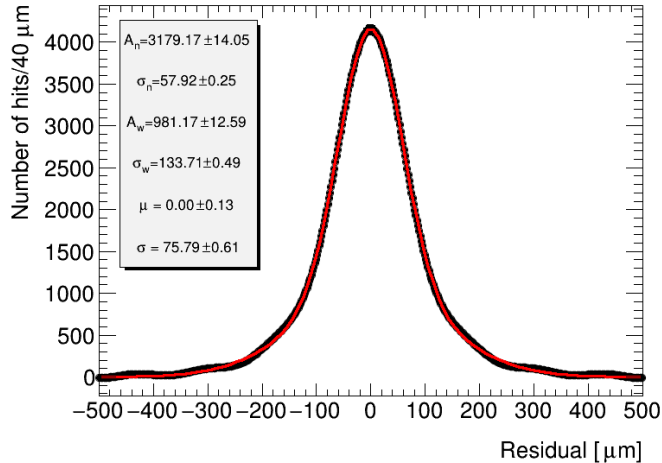


Figure 16: Biased residual distribution after deconvolution of the observed biased residual distribution in figure 10 with the simulated multiple scatter residual distribution in figure 14. Double gaussian fit is red curve with fit parameters as described in Fig. 10 shown in box.

The deconvolution is performed using fourier transforms of the two input distributions. In frequency space, a deconvolution is simply the division of the two histograms. We fourier transform the observed residuals, divide by the fourier transform of the MC truth multiple scattering distribution, and then take the inverse fourier transform of the result. This result of the deconvolution procedure is shown in figure 16.

We then perform a similar procedure to the deconvolution using a convolution to smear the residuals with the multiple scattering distribution of a sample of pure 20 GeV muons from the MC simulation. 20 GeV muons are chosen to be in accordance with the Run 2 MDT resolution result [8], which placed a 20 GeV p_T cut on their muons. Muons with 20 GeV of p_T have at least 20 GeV

of energy, so the 20 GeV monochromatic sample we used was conservative compared to the actual spectrum used in the Run 2 MDT resolution measurement. The multiple scattering is much less for this sample, but is still significant enough to change the overall resolution by 3-4 microns.

4 Systematic Uncertainty Estimation

4.1 Auto-calibration and $r(t)$ parameterization

The choice of Chebyshev polynomials, and the exact value of the coefficients, is a potential source of systematic uncertainty. In order to assess the reproducibility of the auto-calibration algorithm we ran the algorithm on independent data sets and compared the resulting $r(t)$ functions. The results are shown in figure 17. Differences in $r(t)$ functions are on the order of 5-10 microns for the majority of the drift time phase space. In order to assess the impact on the final resolution result we again calculated the residual distributions (figures 10 and 11) but used an $r(t)$ function from a different data partition. We then applied the usual deconvolution, convolution, and resolution calculation and find the maximum change in resolution is $0.3 \mu\text{m}$. This is the uncertainty estimate for the Chebyshev parameterization and auto-calibration routine.

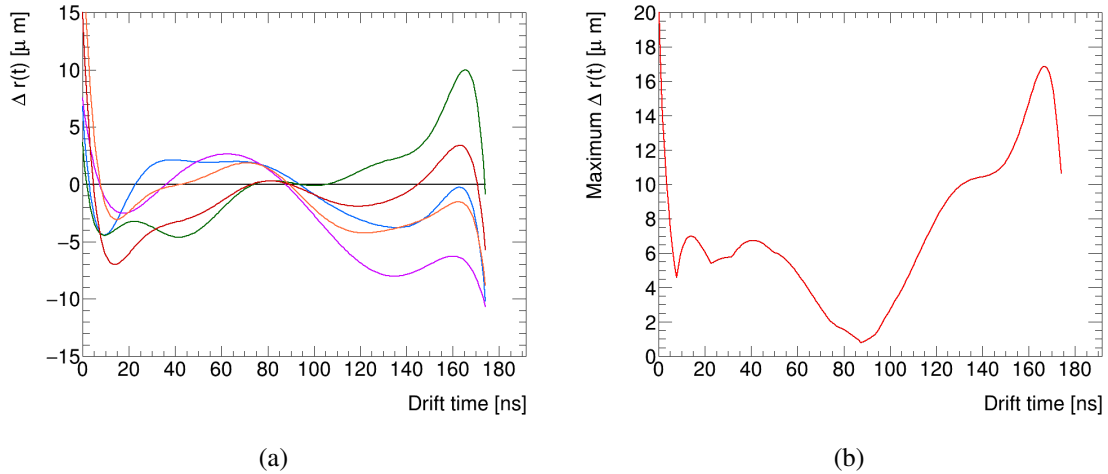


Figure 17: (a) Difference in $r(t)$ function calculated on orthogonal data partitions. Differences are generally on the order of 5-10 microns. (b) Maximum difference between any two data partitions. Differences are greatest near the wire and tube wall, but are again on the order of 5-10 microns for the majority of the drift time phase space.

4.2 Track Fitting

In order to calculate the uncertainty associated with the particular choice of best fit track parameters we used the likelihood ratio technique. We varied the track parameters (Δt_0 , angle, and impact parameter) up and down, optimizing the value of the parameter until the likelihood ratio was consistent with a one standard deviation ratio ($-2\Delta \ln(\lambda) = 1$). For a more detailed description of the likelihood ratio procedure, see appendix B. The size of the perturbation in each parameter

required to shift the likelihood by one sigma is shown in table 2. Figures 18, 19, and 20 show the distribution of these perturbations. After perturbing the track parameters, we recreated the biased and unbiased residual distributions. Figure 21 shows the perturbed biased residual distribution with the impact parameter adjusted up by one standard deviation.

The next step was to run the familiar resolution algorithm on the new residual distributions (deconvolution and convolution included to account for multiple Coulomb scattering). We found that systematically varying the track parameters by one sigma can modify the resolution by up to 5.5 μm . See table 2 for a complete summary of how the individual parameters impact the resolution.

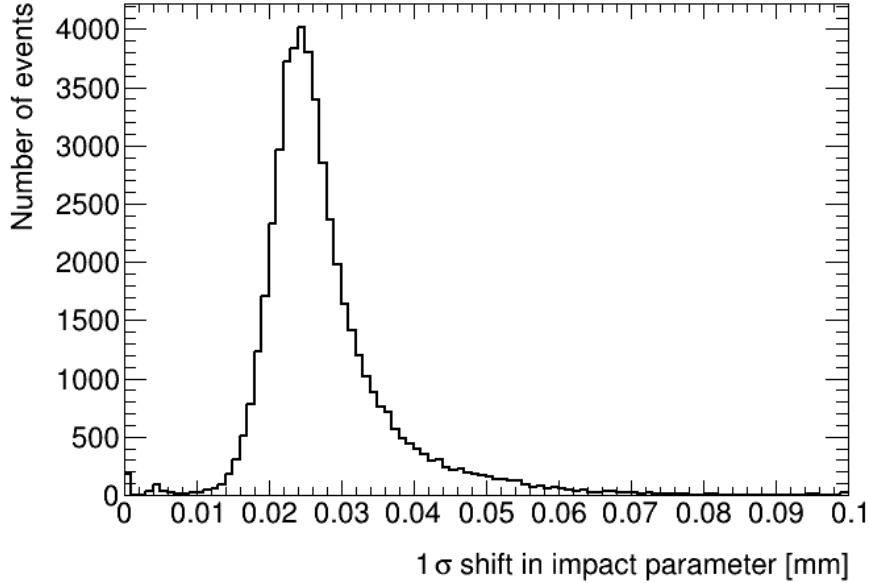


Figure 18: Size of impact parameter shift that produced a one sigma likelihood ratio.

Track Parameter	Mean 1 sigma deviation	Change in resolution
Δt_0	0.81 ns	0.4 μm
b	28 μm	5.2 μm
θ	140 μrad	5.5 μm

Table 2: Mean size of systematic shift for track parameters and impact on resolution.

4.3 Soft-Electron Component of Cosmic-Ray Spectrum

In this section we will estimate the systematic effects of the MC procedure. The primary nuisance parameter is the soft-electron component of the cosmic-ray spectrum, which was nominally chosen to be 30%. The deconvolution procedure also introduces some systematic uncertainties in the Fourier transform, because the result needs to be passed through a low-pass filter to remove noise. The noise is the result of dividing two doubles near the limit of precision, essentially a 0/0 calculation, in some bins. We assess the uncertainty associated with the low-pass cutoff and the cosmic-ray electron component simultaneously by varying the soft-electron fraction to 25 and 35% of the total

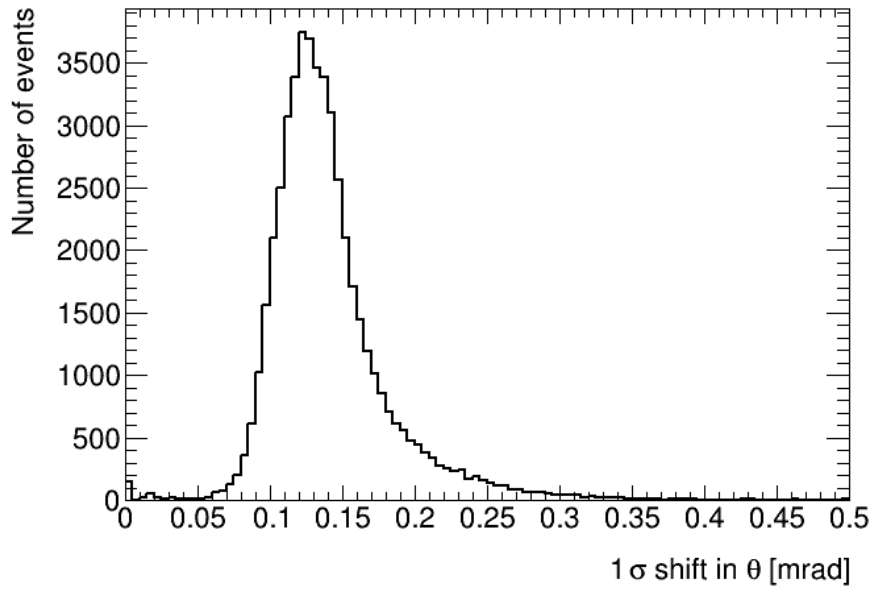


Figure 19: Size of angular shift that produced a one sigma likelihood ratio.

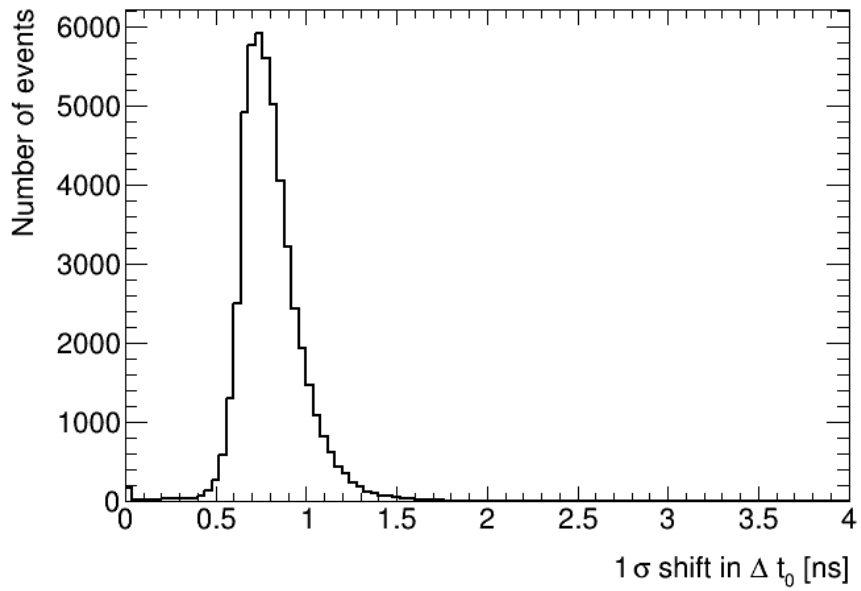


Figure 20: Size of Δt_0 shift that produced a one sigma likelihood ratio.

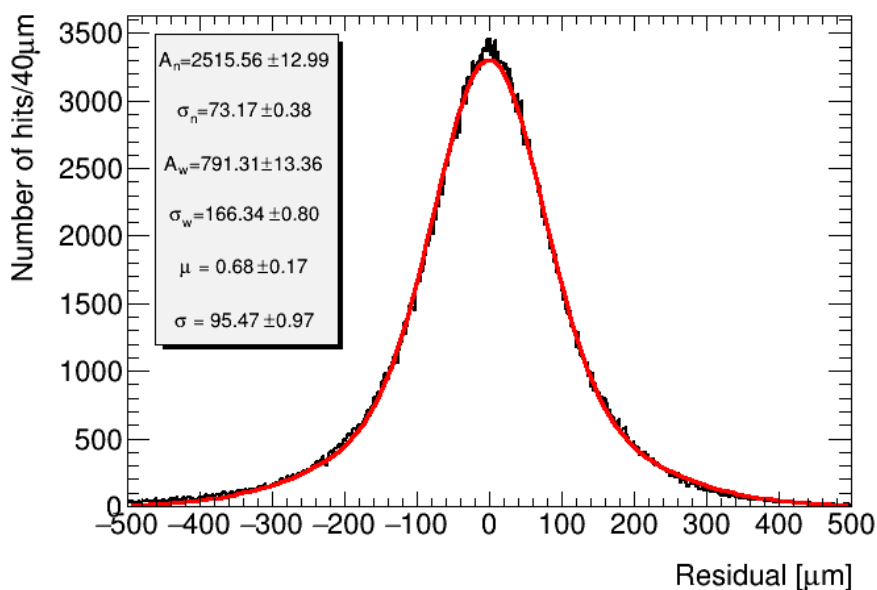


Figure 21: Systematically varied residual distribution with impact parameter shifted up by one sigma. The resulting distribution is slightly wider than the nominal case in figure 10. The red curve is a double gaussian fit as described in section 2.

spectrum and re-computing the deconvolution and final resolution. To be especially conservative we even vary the soft-electron component down to 0%, and we find that the change in single-hit resolution is small. The maximum variation in resolution observed was 1.7 μm . While this may seem small given that electrons are low energy and thus expected to scatter more, a significant fraction of electrons are so low energy that they do not penetrate the entire chamber and pass reconstruction cuts.

4.4 Time Slew Correction

The adopted values for the time slew correction function shown in equation 2.1 have uncertainty. In order to estimate the size of this uncertainty we plot the inverse ADC dependence of the residuals before and after applying the time slew correction in figures 22a and 22b, respectively. The ideal time slew correction would have a slope of zero in the straight line fit in figure 22b. However, a slight correlation remains after applying our time slew correction. Figures 22c and 22d show the relationship between residuals and ADC with the amplitude of the time slew correction varied down or up by 25%, respectively. The 25% variation is large enough that the straight line fits plotted in figures 22c and 22d have slopes of opposite sign, showing that our chosen systematic variation is large enough to account for the degree to which our choice of time slew correction amplitude is non-optimal. Therefore we adopt a conservative upper limit of 25% as the uncertainty on the amplitude of the time slew correction.

The uncertainty in the amplitude of the time slew correction is propagated to the resolution by taking the maximum difference between the resolution measured using the nominal time slew

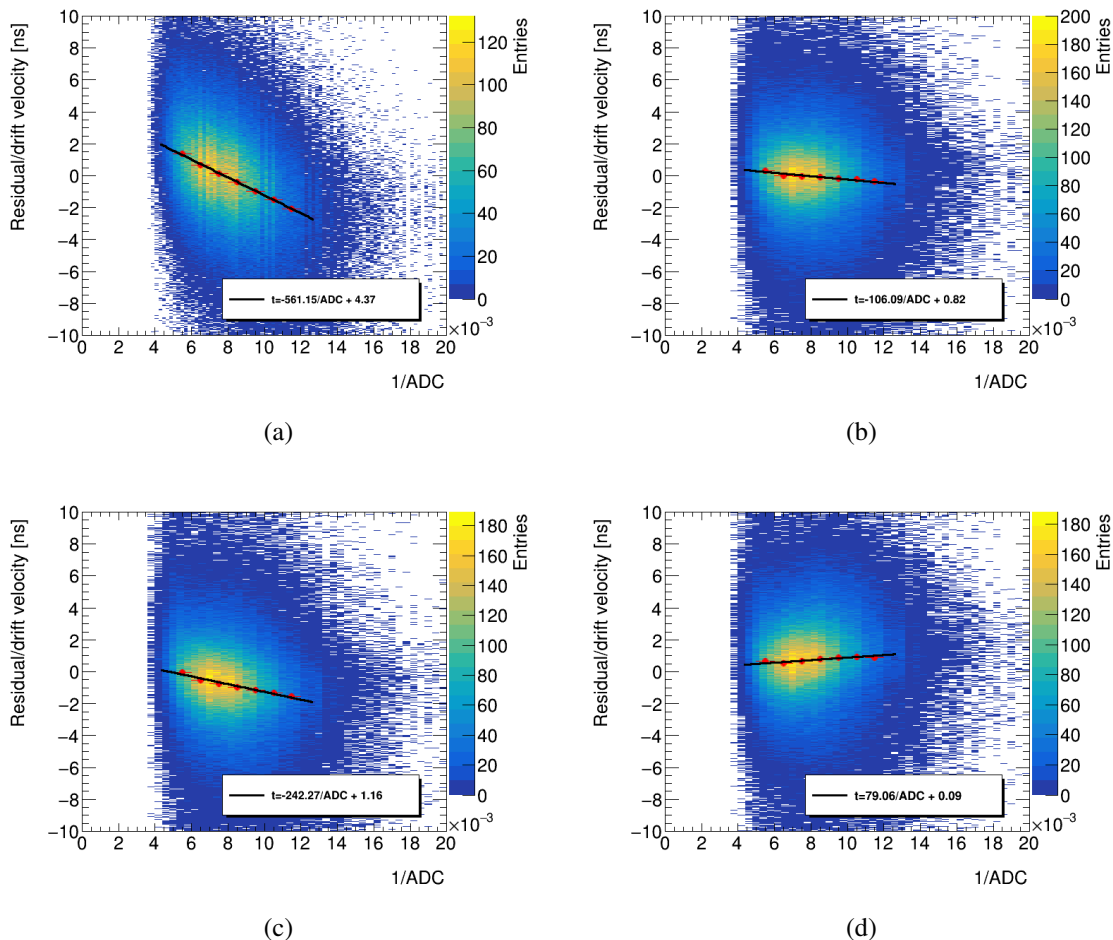


Figure 22: ADC dependence of residuals (a) before and (b) after applying time slew correction, as well as with the amplitude of the time slew correction varied 25% (c) down and (d) up. The residuals are divided by the average drift velocity to put the y axis in units of nanoseconds. The red dots show the mean residual/drift velocity in coarse bins and the black line is a straight line fit to this coarsely binned data. The text boxes show the equations found for the straight line fits.

correction and the two systematic variations, with amplitude varied up and down by 25%. The impact on the resolution is $3.7 \mu\text{m}$.

4.5 Signal Propagation Time

Due to the large ($\approx 1.5 \text{ m}^2$) single trigger scintillator we do not have second coordinate (the position of the particle along the wire) information in this analysis. Second coordinate information is provided by a setup like the one in the ATLAS muon spectrometer, where thin-gap chambers or resistive plate chambers provide additional information about the location of the muon along the direction of the wire. Tracks that are not perpendicular to the wires have their drift times smeared due to disparities in signal propagation time. The mean signal propagation time is already accounted for in our event-by-event Δt_0 parameter.

The two ingredients necessary to characterize signal propagation time are speed and distance. First, we address signal propagation speed. A coaxial transmission line like our drift tubes has a signal propagation speed affected by two factors: (i) the dielectric medium and (ii) the skin depth correction. The dielectric medium used in this analysis is a 93:7 % admixture of argon and carbon dioxide at 3 bars absolute pressure. Argon gas does not have a permittivity or permeability meaningfully different than the vacuum. Therefore, we do not address this affect, but concentrate on the skin depth correction.

The inductance per unit length of a coaxial cable is [14]:

$$\frac{L}{l} = \frac{\mu}{2\pi} \ln\left(\frac{r_t}{r_w}\right) + \frac{\mu_e \delta}{4\pi} \left(\frac{1}{r_w} + \frac{1}{r_t}\right) \quad (4.1)$$

where μ is the permeability of the dielectric medium, μ_e is the permeability of the conductor, r_t and r_w are the inner radius of the tube and outer radius of the wire, respectively, and δ is the skin depth. Given the approximation that all permeabilities in the setup are near that of the vacuum, we can recast this equation to another form and plug in the geometric constants:

$$L = L_0 \left(1 + \frac{\delta}{125\mu\text{m}}\right) \quad (4.2)$$

This correction to the inductance will modify the propagation speed of signals in the tube according to [13, 14]

$$v = 1/\sqrt{LC} = c/\sqrt{L/L_0} = c/\sqrt{1 + \frac{\delta}{125\mu\text{m}}} \quad (4.3)$$

The value for skin depth is dependent on both frequency and material as [13, 14]:

$$\delta = \sqrt{\frac{2\rho}{\omega\mu}} \quad (4.4)$$

Where ρ is the resistivity of the material and ω is the angular frequency of the signal. At 1 MHz, the skin depth of aluminum is calculated to be 84 microns. Plugging this value in to equation 4.3, we find a signal propagation speed of 77% the speed of light. The signal propagation speed is not strongly dependent on the frequency assumed, and changing the assumed frequency by a factor of two only changes the calculated propagation speed by about 5%.

With an estimate of the signal propagation speed we can create a simulated distribution of the change in residuals due to signal propagation effects. The distribution of changes in residuals due to a finite signal propagation speed is analogous to the MC truth multiple scattering distribution shown in figure 14. The procedure is as follows. Draw a random angle from a $\cos^2 \theta$ distribution [13], up to the maximum geometric angular acceptance (defined by total chamber height and length of wires). The $\cos^2 \theta$ assumption is conservative and will overestimate the error because the acceptance for large angles is smaller due to geometric phase space considerations. Calculate the signal propagation distance for each hit as a function of θ and subtract off the mean propagation distance (as the mean propagation time is already accounted for by the Δt_0 parameter). Using the signal propagation speed, convert the distance to a signal propagation time. The signal propagation time has a standard

deviation of about 0.4 nanoseconds. Then, assuming hits are uniformly distributed in radius, choose a random radius between 0 and the inner tube radius, and use the $r(t)$ function derived in section 2 to calculate the difference in measured radius if the timing was displaced by the signal propagation time. Hits at small radii will be more sensitive to changes in timing because the drift velocity is larger near the wire. The resulting distribution is plotted in figure 23. We deconvolute the resulting hit and fit residuals with this histogram, and find a change in resolution of $2.2 \mu\text{m}$. Thus, $2.2 \mu\text{m}$ is the systematic uncertainty envelope associated with the signal propagation timing.

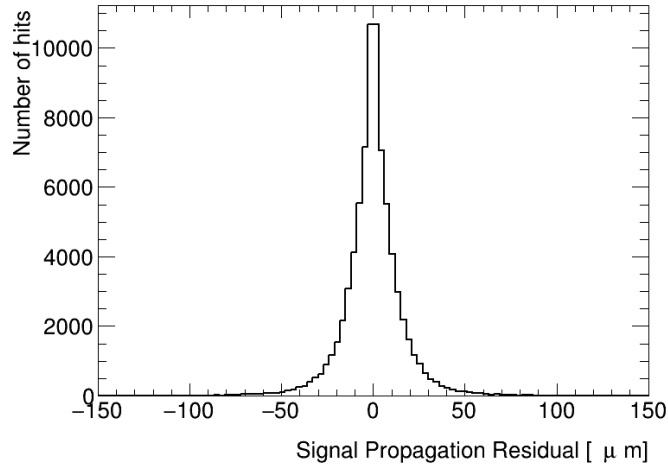


Figure 23: The difference in residual when applying a signal propagation correction, assuming a $\cos^2 \theta$ angular distribution and uniformly distributed drift radii.

In order to double check this theoretical estimation of the signal propagation uncertainty we collected data using a smaller scintillator in the trigger to reduce the angular spread. The methodology presented thus far has used a scintillator on the same order of the size of the chamber (about 1.5 square meters), and the smaller scintillator is about 20 centimeters on each side. The data quality using this scintillator is worse because the hit rate is reduced by a factor of about 50 and much longer data-taking times are required. Data must be taken over several days to accumulate statistics, rather than just a few hours. Temperature and humidity conditions fluctuate enough in the ten days of data taking time that one $r(t)$ function cannot accurately describe the data. Therefore, we observed markedly wider residual distributions. However, we can observe the difference in width between the residual distributions for hits in the top layer, closest to the scintillator, and the bottom layer, farthest from the scintillator. We expect that the signal propagation time will be much more constrained in the top layer than the bottom layer, leading to a wider residual distribution. Since the scintillator is 20 cm long, there is still a small amount of signal propagation smearing in the top layer, but it is reduced by roughly 83% since the new scintillator is only 17% the length of the tube. We observe that the resolution in the top layer is $1.9 \mu\text{m}$ narrower than the resolution measured in the bottom layer. This is consistent with the $2.2 \mu\text{m}$ result obtained via theoretical calculations. Therefore, with empirical evidence and supporting calculations, we conclude that the signal propagation uncertainty is $2.2 \mu\text{m}$.

4.6 Systematic uncertainties on efficiency measurement

A possible source of systematic bias in the efficiency measurement is the fact that we average the efficiency of all 8 layers. Cosmic-rays are incident from above. If there are soft particles (i.e. electrons) that can penetrate some but not all of the layers, it is possible that the efficiency is a function of the number of layers penetrated. We plot efficiency within the gas volume as a function of the number of layers penetrated in figure 24 (geometric inefficiencies are not a function of layers penetrated). Note that we are plotting the tube efficiency and not the layer efficiency. The constant fit with error bars is also plotted. The constant fit has a chi-square per degree of freedom of 0.45, and is not significantly different than the observed data. Therefore we do not adopt any systematic uncertainty regarding the efficiency as function of the number of layers penetrated, as if a relationship exists we are not sensitive to it with the current level of statistics.

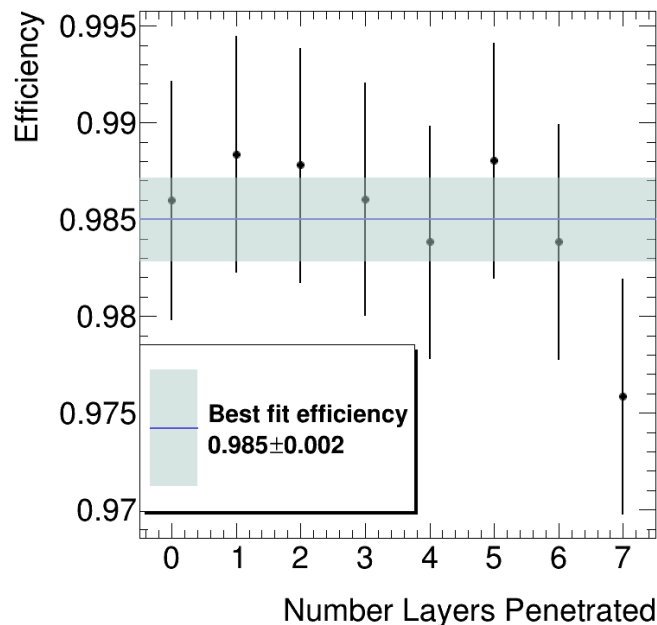


Figure 24: Efficiency within the gas volume measured as a function of the number of layers penetrated. 0 layers penetrated corresponds to the top layer, 1 to the second from the top layer, and so on. The constant fit has a chi-square per degree of freedom 0.45, and is not in tension with the data. We do not adopt a systematic uncertainty in this case.

5 Results

5.1 Single-Hit Resolution

As discussed in section 2.4, the resolution of the BMG prototype chamber was observed to be $117.7 \pm 2.1 \mu\text{m}$ (statistical uncertainty only) without accounting for multiple scattering effects. When both the biased and unbiased residuals were deconvoluted using the procedure outlined in section 3.3 the resolution improved to $103.7 \pm 3.5 \mu\text{m}$. Accounting for the systematic uncertainty

Uncertainty	Prototype chamber	Module 0
Statistical	3.5 μm	2.4 μm
Track Fit Parameters Error Propagation	5.5 μm	5.2 μm
Soft-Electron Component in MC simulation	1.7 μm	3.0 μm
Signal Propagation Time	2.2 μm	3.3 μm
Time Slew Correction Normalization	3.7 μm	2.8 μm
r(t) parameterization	0.3 μm	0.3 μm
Total	8.1 μm	7.8 μm

Table 3: Summary of error bars for single-hit resolution measurement. Total error is obtained by adding the individual errors in quadrature.

described in section 4 the observed resolution is $103.7 \pm 8.1 \mu\text{m}$. See figure 27a for a comparison of the resolution of the test chamber and module 0 with the Run 2 MDT result for reference [8]. Notably, the ASD 2 chip achieves finer resolution due to its higher gain. When using legacy ASD chips on module 0 we observed a resolution of $101.8 \pm 7.8 \mu\text{m}$ and the ASD 2 chip improved the resolution to $90.0 \pm 7.8 \mu\text{m}$. The ASD 2 chips will be used on sMDT chambers installed in the ATLAS detector, and will be installed on all existing ATLAS MDT chambers in the ATLAS Phase 2 upgrade in 2024.

The systematic uncertainties for both chambers are summarized in table 3. The systematic uncertainties are different due to the differing geometry of the two chambers and the different readout electronics (ASD 1 vs 2). While the two chambers are very similar (same operating voltage, tube radius) there are geometric differences that can subtly impact the performance (most notably that the two multilayers are approximately 15 cm closer in module 0 as compared to the BMG-like prototype). Chambers are designed with different geometries in order to fit in various locations within the ATLAS muon spectrometer.

We have also calculated the resolution as a function of radius. We binned the biased and unbiased residuals for both the MC truth and observed data in 1mm radial bins and performed the deconvolution procedure in each bin. The resulting resolution vs radius curve is shown in figure 25. The resolution vs radius plots have been fit with a second order polynomial whose coefficients are summarized in table 4. As discussed in section 2, the resolution procedure is performed iteratively until the coefficients in table 4 converge. The coefficients define the error on a hit, depending on its radius.

Parameter	Prototype Chamber Value [μm]	Module 0 Value [μm]
c_0	195.3 ± 10.9	185.6 ± 10.6
c_1	-31.5 ± 6.5	-39.4 ± 6.4
c_2	2.0 ± 0.9	3.4 ± 0.8

Table 4: Fitted polynomial coefficients for the residual vs. radius curve, a function of drift distance (measured in mm).

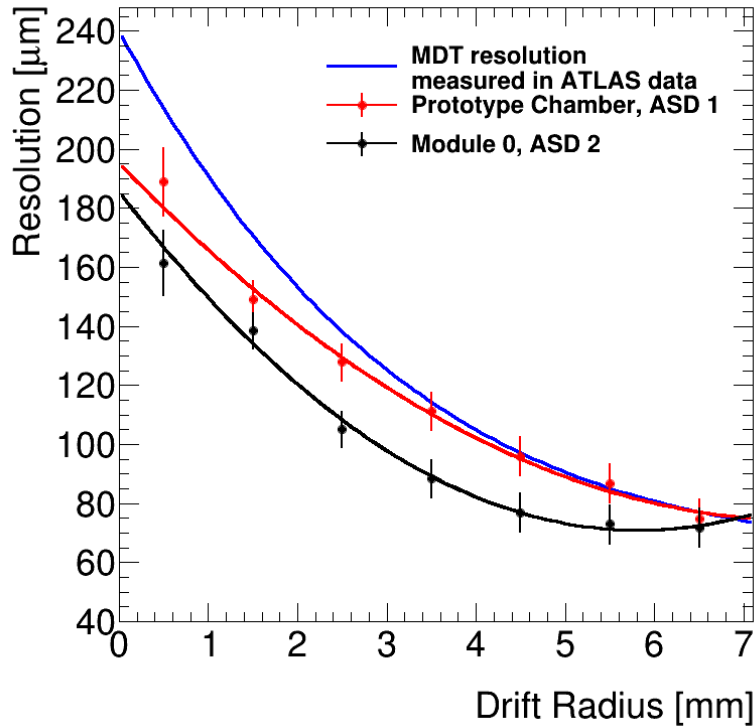


Figure 25: Observed resolution as a function of radius, after performing the deconvolution technique to remove the effects of multiple scattering. For comparison we show the best fit curve observed in the Run 2 MDT resolution study.

5.2 Efficiency

Using data taken on the prototype sMDT chamber the measured (expected) layer efficiency is 0.942 ± 0.002 (0.94) [4]. The measured tube efficiency (when only considering the active gas volume of the tubes) is 0.985 ± 0.002 . figure 26 shows the efficiency as a function of drift radius, which demonstrates that the region near the tube wall is responsible for most of the inefficiency of the chamber, other than the intrinsic geometric inefficiency due to spacing between the gas volumes. Similar results are achieved with the module 0 chamber.

We did not observe any relationship between efficiency and the number of layers penetrated, so the quoted efficiency is an average of all 8 layers. See figure 27b for a comparison of the efficiencies measured on the test chamber and module 0.

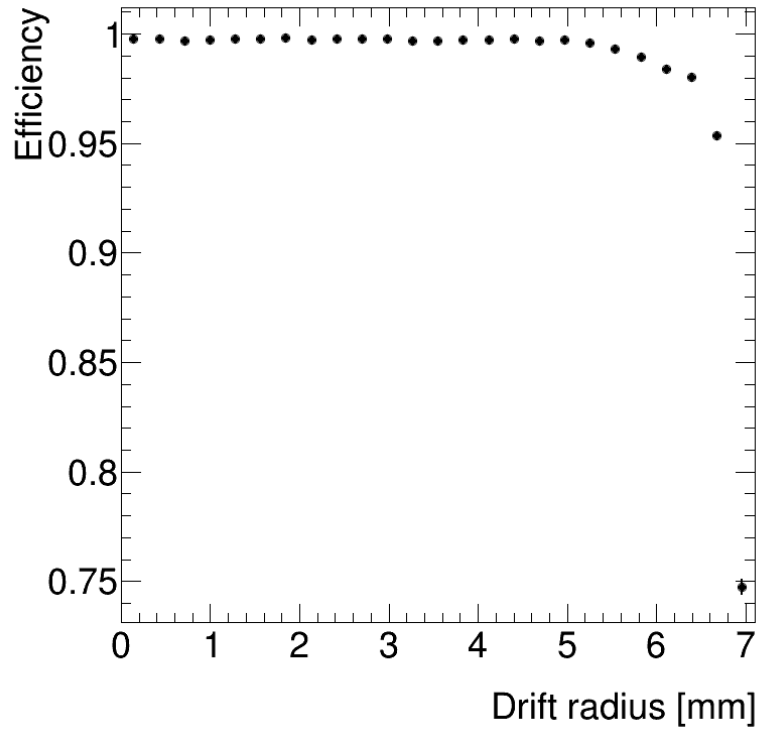


Figure 26: Efficiency as a function of drift radius shown with statistical error bars measured on the BMG prototype chamber. The region near the tube wall is responsible for most of the inefficiency of the chamber within the gas volume. The 0.9 mm gap between gas volumes, consisting of the two 0.4 mm tube walls and the 0.1 mm space between tubes, is the reason for the rest of the inefficiency.

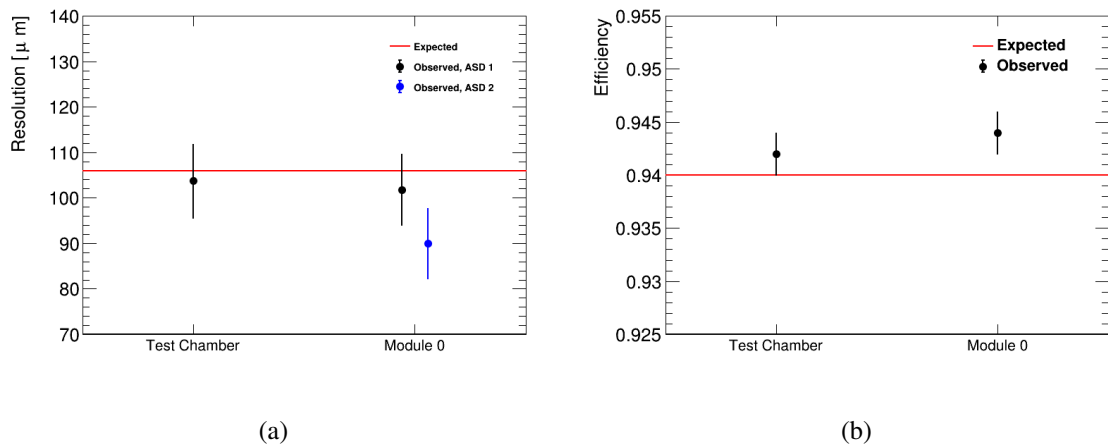


Figure 27: (a) Measured resolution for test chamber and module 0. Module 0 resolution measured with both legacy electronics (ASD 1) and the new ASD 2 chips, which have higher gain. (b) Measured efficiency for test chamber and module 0

6 Conclusions and Future Work

We observe a resolution of $103.7 \pm 8.1 \mu\text{m}$ for the BMG test chamber, consistent with the expected resolution of $106 \mu\text{m}$. This result, including the assessment of the resolution and the size of the multiple scattering effect, is consistent with other studies of sMDT performance [15, 16]. Three crucial components of the analysis strategy were the in-situ $r(t)$ function, the addition of a Δt_0 parameter and accounting for multiple scattering via Geant simulation. The $r(t)$ was determined by an auto-calibration using a matrix-inversion technique with an initial $r(t)$ provided by the ATLAS gas monitor chamber. The addition of the Δt_0 parameter is necessary to account for trigger timing smeared by a large trigger scintillator. The convolution procedure was motivated by the Monte Carlo simulation, which showed a significant difference in multiple scattering for cosmic-rays and 20 GeV muons. By accounting for multiple scattering we were able to measure the prototype BMG chamber resolution as it would perform on muons with 20 GeV of p_T in the ATLAS detector to be $103.7 \pm 8.1 \mu\text{m}$, to be compared with an expected resolution of $106 \mu\text{m}$. We also measured a resolution of $101.8 \pm 7.8 \mu\text{m}$ on the BIS module 0 chamber, which was improved to $90.0 \pm 7.8 \mu\text{m}$ with the use of the higher gain ASD 2 chips. The measured efficiency was 0.942 ± 0.002 (0.944 ± 0.002) for the BMG (BIS) chamber, consistent with the expected efficiency 0.94. We conclude that the sMDT prototype chambers assembled at the University of Michigan are consistent with the design specifications for resolution and efficiency.

Despite producing a resolution and efficiency measurement on the prototype chamber and module 0, this project is still ongoing. The methodology will be used to measure the resolution of new chambers produced at the University of Michigan. Documentation of the code is available at <https://kenelson.web.cern.ch/documentation/smdt-reco>.

A Matrix Inversion Chi Square Minimization

Both the tracks and $r(t)$ function are optimized using a matrix inversion linearized chi-square method.

The chi-square is the a function of the difference of some measured distance between the hit and wire d_i^{meas} , and the functional form described by the parameters α_μ :

$$\chi^2 = \sum_{i=1}^N \frac{(d_i^{meas} - d_i(\alpha_\mu))^2}{\sigma_i^2} \quad (\text{A.1})$$

Write down the derivative of the chi-square with respect to the parameters and set it equal to zero:

$$\frac{\partial \chi^2}{\partial \alpha_\mu} = -2 \sum_i \frac{(d_i^{meas} - d_i(\alpha_\mu))}{\sigma_i^2} \frac{\partial d_i}{\partial \alpha_\mu} = 0 \quad (\text{A.2})$$

Assuming the initial guess is close to the right answer, high order derivatives can be neglected:

$$d_i \approx d_{0i} + \sum_\mu \frac{\partial d_i}{\partial \alpha_\mu} \Delta \alpha_\mu \quad (\text{A.3})$$

Plug in the linearized residual into the derivative of the chi-square and solve for $\Delta\alpha_\nu$.

$$0 = \sum_i^N \frac{(d_i^{meas} - d_{0i} - \sum_\nu \frac{\partial d_i}{\partial \alpha_\nu} \Delta\alpha_\nu)}{\sigma_i^2} \frac{\partial d_i}{\partial \alpha_\mu} \quad (\text{A.4})$$

$$\Delta\alpha_\nu = - \left(\sum_\nu \sum_i \frac{1}{\sigma_i^2} \frac{\partial d_i}{\partial \alpha_\nu} \frac{\partial d_i}{\partial \alpha_\mu} \right)^{-1} \left(\sum_i \frac{(d_{0i} - d_i^{meas})}{\sigma_i^2} \frac{\partial d_i}{\partial \alpha_\mu} \right) \quad (\text{A.5})$$

This provides a prescription for updating the coefficients α_ν via inverting a matrix of derivatives of the hit distances.

B Likelihood Ratio Technique for Propagation of Errors

During matrix-inversion optimization the track parameters can be tuned to arbitrary precision. This does not reflect the actual uncertainty on the parameters, which can be assessed using the likelihood ratio.

The likelihood of a model is the probability of observing data under the assumptions of that model [17]:

$$\mathcal{L}(\Theta|\vec{x}) = P_\Theta(\vec{x}) \quad (\text{B.1})$$

In this case, the model Θ is the track parameterization and the data \hat{x} are the measured drift radii.

$$\vec{x} = r^{\text{meas}} \quad (\text{B.2})$$

$$\Theta = (\theta, \Delta t_0, b) \quad (\text{B.3})$$

Where θ is the 2-D track angle with respect to the vertical, b is the impact parameter (or x-intercept in figure 8), and Δt_0 is the event-by-event timing shift. The probability of measuring a particular set of gaussian distributed data is

$$P_\Theta(r^{\text{meas}}) = \prod_i \frac{1}{\sigma(r_i^{\text{meas}})\sqrt{2\pi}} e^{-\frac{1}{2} \left(\frac{r_i^{\text{meas}} - r_i^{\text{pred}}(\Theta)}{\sigma(r_i^{\text{meas}})} \right)^2} \quad (\text{B.4})$$

Where $\sigma(r_i^{\text{meas}})$ is the error as a function of drift radius, shown in figure 25, and r_i^{pred} is the predicted radius by the model. The likelihood ratio between two models, Θ and Θ' , is given by

$$\lambda = -2 \ln \left(\frac{\mathcal{L}(\Theta|\vec{x})}{\mathcal{L}(\Theta'|\vec{x})} \right) \quad (\text{B.5})$$

To evaluate the size of the uncertainty on the model parameters, we perturb them up and down from their best fit values until the likelihood ratio equals 1, where the model is in conflict with the best fit by one standard deviation. We then propagate the error on the track parameters by creating residual distributions under the perturbed hypothesis and calculating the change in resolution from the nominal case.

Acknowledgments

We would like to thank Bing Zhou, Curtis Weaverdyck, Xiangting Meng, Jing Li and Zhe Yang for construction of the prototype chamber and initially set up of the DAQ system for this study. We also thank Tiesheng Dai and Zhen Yan for their valuable comments and discussions during conducting this research studies. We thank the DOE for funding the ATLAS research project at Michigan (DOE Grant #: DE-SC007859).

Bibliography

- [1] ATLAS collaboration, *The ATLAS experiment at the CERN large hadron collider*, *JINST* **3** (2008) S08003.
- [2] ATLAS collaboration, *Technical Design Report for the Phase-II Upgrade of the ATLAS Muon Spectrometer*, CERN-LHCC-2017-017.
- [3] ATLAS collaboration, *Technical Design Report for the Phase-II Upgrade of the ATLAS TDAQ System*, CERN-LHCC-2017-020.
- [4] H. Kroha, R. Fakhruddinov and A. Kozhin, *New High-Precision Drift-Tube Detectors for the ATLAS Muon Spectrometer*, *JINST* **12** (2017) 12.
- [5] C. Ferretti and H. Kroha, *Upgrades of the ATLAS Muon Spectrometer with sMDT Chambers*, ATL-MUON-PROC-2015-006.
- [6] J. Christiansen, *HPTDC High Performance Time to Digital Converter*, <https://cds.cern.ch/record/1067476>.
- [7] C. Posch, E. Hazen and J. Oliver, *MDT-ASD, CMOS front-end for ATLAS MDT*, ATL-MUON-2002-003.
- [8] ATLAS collaboration, G. Aad et al., *Resolution of the ATLAS muon spectrometer monitored drift tubes in LHC Run 2*, *JINST* **14** (2019) P09011, [1906.12226].
- [9] O. Kortner, H. Kroha and J. von Loeben, *Calibration of the ATLAS MDT chambers with curved muon tracks*, ATL-COM-MUON-2011-003.
- [10] D. Levin et al., *Drift time spectrum and gas monitoring in the atlas muon spectrometer precision chambers*, *Nucl. Instrum. Meth. A* (2008) .
- [11] M. Frasn, S. Abovyan, V. Danielyan, H. Kroha, S. Nowak, R. Richter et al., *An 8-Channel ASD in 130 nm CMOS for ATLAS Muon Drift Tube Readout at the HL-LHC*, *PoS TWEPP-17* (2018) 004.
- [12] S. Agostinelli, J. Allison, K. Amako, J. Apostolakis, H. Araujo, P. Arce et al., *Geant4-a simulation toolkit*, *Nucl. Instrum. Meth. A* (2003) 250 – 303.
- [13] PARTICLE DATA GROUP collaboration, *Review of particle physics*, *Phys. Rev. D* **98** (2018) 030001.
- [14] J. D. Jackson, *Classical electrodynamics; 2nd ed.* Wiley, New York, NY, 1975.
- [15] K. R. Schmidt-Sommerfeld, *Study of Muon Drift Tube Detectors and Fast Readout Electronics for Very High Counting Rates*, CERN-THESIS-2020-016.
- [16] S. Hadzic, *Test of High-Resolution Muon Drift-Tube Chambers for the Upgrade of the ATLAS Experiment*, CERN-THESIS-2019-150.
- [17] E. L. Lehmann and J. P. Romano, *Testing statistical hypotheses*. Springer Texts in Statistics. Springer, New York, third ed., 2005.